Bathymetric Retrieval Selectively Using Multiangular High-Spatial-Resolution Satellite Imagery

Bin Cao [ORCID], Ruru Deng, Shulong Zhu, Yongming Liu [ORCID], Yeheng Liang, and Longhai Xiong

Abstract—This article introduces multiangular imagery into physics-based bathymetry in order to compensate for the shortage of bathymetric spectral bands caused by the low spectral resolution of current high-spatial-resolution satellite multispectral imagery. The focus is to propose a selective bathymetric retrieval method to eliminate the negative effect of nonoptimal image data on depth retrieval in multiangular imagery-based bathymetry. The elimination of the negative effect is implemented by excluding nonoptimal pixels in every individual image from bathymetric retrieval. An empirical criterion is designed for the determination of nonoptimal pixels. The proposed method can use multiangular image data selectively, avoiding situations where bathymetric retrieval results from the whole multiangular imagery are poorer than that from a part of the individual images. The method was tested in two typical areas within the Xisha (Paracel) Islands of the South China Sea using two-angle WorldView-2 multispectral images. The test showed that the derived depths of the method (i.e., depths derived from the selective image data) provided a better fit to the validation depths than those from the entirety of both images. The underestimation of depths derived from the entirety of both images was also improved to some extent.

Index Terms—Digital depth model (DDM), multiangular imagery, multispectral imagery, nonoptimal image data, physics-based bathymetry, selective bathymetric retrieval.

I. INTRODUCTION

BATHYMETRY is the study of the underwater depth of lake or ocean floors [1]. Satellite-derived bathymetry (SDB) is being widely adopted as a relatively cheap and spatially extensive technique for shallow-water (<20 m) bathymetry [2], [3]. Physics-based bathymetry is one of the most widely used SDB approaches [4]. It can derive bathymetric information from satellite multispectral or hyperspectral imagery with an accuracy of 1–2 m root-mean-square error (RMSE), down to a depth of about 20 m [5]–[11].

Physics-based bathymetry is based on the radiative transfer model (RTM) [12] inversion. It uses an RTM to model a range of possible remote-sensing (RS) reflectance as a function of water quality, water depth, and bottom reflectance. The model is then inverted for each spectral measurement to retrieve model parameters (i.e., the bottom and water column properties, including water depth) [13], [14]. Visible light (especially green and blue light) is usually used for physics-based bathymetry because it has good water penetration characteristics [4], [12]. Shorter wavelength near-infrared (NIR) light is used only occasionally [15] due to its small penetration depth (<1 m). Physics-based bathymetry usually uses multiple spectral bands to derive the depth or to discriminate among substrates [16]–[18]. For bio-optical RTM-based bathymetric retrieval, at least six spectral bands in the visible-to-NIR domain (about 400–800 nm spectral range) are needed because there are at least six unknowns (i.e., six property parameters of the bottom and water column) in the model to be solved [19], [20], implying that only high- and medium-spectral-resolution satellite imagery (at least six bands) can be used for reliable bathymetry.

The spatial resolution of satellite imagery plays a significant role in ensuring the accuracy and reliability of the derived information [21], [22]. It is one of the most important factors in determining the size of the resolution cell of the derived information. To attain higher accuracy, higher spatial-resolution satellite imagery should be used for physics-based bathymetry to the fullest extent possible. Unfortunately, because of technical constraints, a high spatial resolution is always associated with a low spectral resolution and vice-versa [23]. That means a satellite imaging system with a high spatial resolution can only offer a medium or low spectral resolution. Currently, high-spatial-resolution RS satellites (e.g., IKONOS [24], QuickBird [25], GeoEye-1 [26], SPOT 6 and 7 [27], and WorldView-2, 3, and 4 [28]) only provide multispectral imagery with a small number of visible and shorter wavelength NIR bands. Most of them provide four standard visible and near-infrared (VNIR) bands (i.e., blue, green, red, and NIR bands), which are not adequate for solving the bathymetric model with six unknown parameters. Only a few of them provide more than four multispectral bands (e.g.,

Bin Cao, Yeheng Liang, and Longhai Xiong are with the School of Geography and Planning, Sun Yat-Sen University, Guangzhou 510275, China (e-mail: caobinalonzo@sina.com; liangyh28@mail.sysu.edu.cn; xionglh5@mail.sysu.edu.cn).

Ruru Deng is with the Guangdong Engineering Research Center of Water Environment Remote Sensing Monitoring, Guangdong Provincial Key Laboratory of Urbanization and Geo-Simulation, School of Geography and Planning, SunYat-Sen University, Guangzhou 510275, China (e-mail: eesdrr@mail.sysu.edu.cn).

Shulong Zhu is with the College of Data Sciences, Information Engineering University, Zhengzhou 450001, China (e-mail: zhushulong668@sina.com).

Yongming Liu is with the State Key Laboratory of Tropical Oceanography, Guangdong Key Laboratory of Ocean Remote Sensing, South China Sea Institute of Oceanology, Chinese Academy of Sciences, Guangzhou 510301, China (e-mail: liuyongminga401@outlook.com).

WorldView-2 and 3 offer eight multispectral bands, including four standard VNIR bands and four special bands). Those RS satellites do not provide sufficient bathymetric spectral bands because they are not designed only for bathymetry. The low spectral resolution is a limiting factor in bathymetric retrieval based on the bio-optical RTM. One challenge is that insufficient bathymetric spectral bands may result in unreliable bathymetric retrievals [29].

Fortunately, some high-spatial-resolution satellites have high pointing agility that enables them to take images of the same area of interest in a single pass using different view angles [28]. The multiview imagery of the same area of interest, acquired through cross-track or along-track imaging mode using different view angles, is referred to as multiangular imagery. Such an imagery includes more different observations of targets than a single-view imagery or multiview imagery acquired using the same view angles. Although the band number of multi-angular satellite multispectral imagery has not increased, the increased different observations are helpful for physics-based bathymetry [15]. It is necessary to introduce multiangular RS data into physics-based bathymetry in order to compensate for the shortage of bathymetric spectral bands caused by the low spectral resolution of current high-spatial-resolution satellite multispectral imagery.

This article presents a multiangle bathymetric retrieval method in which the multiangular RS data are used for physics-based bathymetry. The bathymetric retrieval algorithm is based on a bio-optical RTM [19], [30] and multiangular multispectral imagery. There are six unknown model parameters to be solved for every water bottom point, which are related to the water and bottom properties, including the water depth. Thus, two high-spatial-resolution multispectral images, acquired with different view angles, can basically satisfy a requirement of solving the model with six unknown parameters.

Multiangular imagery consists of multiple (two or more) images acquired with different view angles, some of which may be useless for inferring bathymetry or even diminish the contribution of other individual images to bathymetric retrieval. Nonoptimal images refer to those that are useless or have a negative effect on bathymetric retrieval. If multiangular satellite imagery includes nonoptimal individual images, the bathymetric results derived from the whole multiangular imagery might be worse than those from all the individual images, excluding the nonoptimal ones. Nonoptimal images might be caused by sun elevation and azimuth, nonoptimal satellite sensor pointing and sun-sensor-target geometry, environmental noise (e.g., water surface glint [31]), atmospheric path scattering, and/or non-ideal bottom reflection properties. The effect of atmospherically degraded imagery on bathymetric retrieval can be removed by atmospheric correction during image preprocessing [19], [32], [33]. The effect of image quality caused by sun elevation and azimuth, satellite sensor pointing, sun-sensor-target geometry, bottom reflection properties, and water surface glint on bathymetric retrievals is very complex [34]. So far, there is no effective algorithm that can eliminate that effect. Botha *et al.* [34] examined and quantified the effect of image quality caused by variations in sun-sensor-target geometry on bathymetric retrievals, showing that depths were underestimated from the imagery close

to the specular point of the bidirectional reflectance distribution function. Lee *et al.* [15] analyzed the effect of varying view angles on bathymetry derivation and found that images acquired at more off-nadir view angles had a lower correlation with the actual bathymetry data. Jawak *et al.* [4] pointed out that the light is entirely reflected off the water surface at high angles of incidence, preventing any observation of underwater features. Kay *et al.* [31] mentioned that sun glint is a serious confounding factor for RS of water column properties and bottom features, and an uncorrected glint in high-resolution imagery will lead to errors as large as 30% in the measurement of water depth. The existing studies showed that the negative effect of nonoptimal images on bathymetric retrieval exists and varies spatially within an image scene. The effect must be taken into account when multiangular imagery is used for bathymetric retrieval.

To eliminate the negative effect of nonoptimal images on bathymetric retrievals, this article proposes a selective bathymetric retrieval method that can automatically exclude nonoptimal image data from multiangular imagery in per-pixel retrieval. The bathymetric information of every pixel is derived from all the optimal and near-optimal image pixel data. Two typical areas were selected to test the selective bathymetric retrieval method. WorldView-2 was used not only because it is a typical high-resolution commercial RS satellite but also because it can provide two-angle multispectral images for the two study areas. Its stereopairs contain ideal two-angle images that are collected on the same satellite orbit with different view angles. The experiments focused on the comparison between the results obtained by the proposed method (i.e., results obtained after removing the nonoptimal pixels) and the results derived from the entire two-angle image dataset (including nonoptimal pixel data) in order to observe the changes caused by the exclusion of nonoptimal pixels. The study also analyzed what caused nonoptimal pixels and why the proposed method gave the desired bathymetric retrieval results.

II. METHODS AND MATERIALS

A. Bathymetric Retrieval Algorithm Based on Bio-Optical RTM and Multiangular Imagery

1) Bio-Optical RTM Used in This Research: To efficiently simulate a range of spectral reflectance of optically shallow water, this article uses a bio-optical RTM that describes reflectance as a function of properties of the bottom (depth and reflectance) and the water column (absorption and backscattering coefficients) as follows [13], [19], [30], [35]–[38]:

$$R = \frac{0.5r}{1 - 1.5r} \tag{1}$$

$$r = r^{\mathrm{dp}}\left[1 - e^{-\left(\frac{1}{\cos\theta_{\mathrm{sun}}} + \frac{D^c}{\cos\theta_{\mathrm{view}}}\right)\cdot k\cdot H}\right]$$
$$+ \frac{\rho}{\pi}e^{-\left(\frac{1}{\cos\theta_{\mathrm{sun}}} + \frac{D^b}{\cos\theta_{\mathrm{view}}}\right)\cdot \kappa\cdot H} \tag{2}$$

where R and r are the above-surface and subsurface RS reflectance, respectively; r^{dp} is the subsurface RS reflectance of the optically deep water (where bottom reflectance is negligible); D^c and D^b are the optical path-elongation factors for scattered

photons from the water column and the bottom, respectively; κ is the attenuation coefficient of light through water; H is the water depth; ρ is the bottom albedo; θ_{sun} is the subsurface solar zenith angle; and θ_{view} is the subsurface view zenith angle. Note that R and r are the functions of wavelength.

Equation (1) accounts for the cross-surface impact that includes water-to-air transmission as well as subsurface internal reflection. The first and second terms on the right side of (2) represent the contribution from the water column and the bottom, respectively. The above-surface RS spectral reflectance can be further expressed as a function of wavelength λ and RTM parameters P, G, X, Y, H, and B, i.e.,

$$R(\lambda) = f_1(\lambda, P, G, X, Y, H, B) \tag{3}$$

where P is the phytoplankton absorption coefficient at 440 nm, G is the gelbstoff absorption coefficients at 440 nm, X is the backscattering coefficient of suspended particles at 400 nm, Y is the spectral shape parameter, H is the water depth, and B is the bottom albedo value at 550 nm [39].

2) Bathymetric Retrieval Algorithm Based on Multiangular Imagery: Spectral reflectance for a given band is defined as the band-averaged spectral reflectance [30]. Therefore, the above-surface RS spectral reflectance at band b_i is just a function of six RTM parameters related to the water and bottom properties, i.e.,

$$R(b_i) = f_2(P, G, X, Y, H, B). \tag{4}$$

For the application of multiangular multispectral imagery to bathymetric retrieval, another index j, representing the jth sensor view direction, is introduced into (4). Thus

$$R_j(b_i) = f_2(P, G, X, Y, H, B) \tag{5}$$

where $R_j(b_i)$ represents the spectral reflectance at the ith band in the jth sensor view direction. Equation (5) assumes that the properties of the bottom and the water columns are the same at different observation angles. This assumption is applicable for shallow-water bathymetry in the case that the multiangular imagery used is acquired in a single satellite pass because only a small water area and a short time interval are involved in the multiangle imaging.

When multiangular n-band multispectral imagery, acquired with m different view angles, is used for bathymetric retrieval, every bottom point within the image overlap area corresponds to m conjugate image points and $m \times n$ spectral reflectance measurements. Note: Conjugate image points correspond to the same object point on different images. Thus, the six RTM parameters (i.e., P, G, X, Y, H, and B) of every bottom point can be estimated by minimizing the following error function:

$$\varepsilon = \frac{\sqrt{\sum_{j=1}^{m} \sum_{i=1}^{n} \left(R_j^{\mathrm{image}}(b_i) - R_j^{\mathrm{model}}(b_i) \right)^2}}{\sum_{j=1}^{m} \sum_{i=1}^{n} R_j^{\mathrm{image}}(b_i)} \tag{6}$$

where $R_j^{\mathrm{image}}(b_i)$ is the spectral reflectance calculated from image digital number (DN) values in the ith band of the multispectral imagery acquired with the jth group of view angles,

and $R_j^{\mathrm{model}}(b_i)$ is the spectral reflectance at the ith band in the jth view direction calculated by substituting the approximate values of P, G, X, Y, H, and B into (5). The conversion from image pixel values to band-averaged spectral reflectance (i.e., spectral reflectance at a given band) can be seen in the WorldView-2 technical note [40]. The optimization is implemented by the hyperspectral optimization process exemplar [41], which does not require the difficult estimation condition that any parameter value in the estimation range has the same probability. The estimation is a process of iterative optimization. The initial value of H has a greater impact on the estimation accuracy than those of the other parameters. Therefore, this article generates multiple results using different initial values for H and using constant initial values for other parameters, and takes the result of minimizing the error function, as the final one.

The bathymetric model, i.e., (5), gives a unified form for single and multiangular imagery. Taking $j = 1$ gives a bathymetric model for single imagery. Taking j as any integer greater than 1 gives a bathymetric model for multiangular imagery. Note that a single multispectral image can satisfy a requirement of solving the bathymetric model only when band number n is greater than or equal to six (the number of the unknown parameters).

In contrast to single imagery-based bathymetric retrieval, the determination of conjugate image points on multiangular imagery is required for multiangular imagery-based bathymetric retrieval. The determination of conjugate image points is usually performed using the blue or green bands of multiangular imagery because bottom features at a broad range of depths are more visible at those two wavelengths. To deal with radiometric distortion and weak bottom reflectance signal [42] caused by water circumstances, as well as the occlusion of features [43], this article uses a combination of semiglobal matching (SGM) [44], [45] and scale-invariant feature transform (SIFT) [46] algorithms to determine dense conjugate image points with a subpixel accuracy. The SGM algorithm is used to generate dense and reliable disparity maps because it can compensate for radiometric differences of input images by using a pixel-wise mutual information-based matching cost [44]. The SIFT algorithm is used to provide accurate local feature points for correcting wrong disparities in weak texture or occluded areas generated by the SGM algorithm. Cao *et al.* [47] described the detailed procedure of the combined algorithms and showed the practical performance.

B. Exclusion of Nonoptimal Image Data

As mentioned in Section I, the selective bathymetric retrieval method needs to exclude nonoptimal image data from the multiangular image data on a per-pixel basis. The bathymetric information of every pixel is then derived from all the remaining optimal and near-optimal image pixel data. The exclusion is performed independently for each pixel. An empirical criterion is used for the exclusion. The multispectral data of a pixel in a single multispectral image are excluded from bathymetric retrieval (i.e., the pixel data are not used for depth retrieval) when the ratio of the logarithm-transformed spectral reflectance

at the blue band to that at the green band is less than the average ratio of all the conjugate pixels in the multiangular imagery, i.e.,

$$\frac{\ln\left(q \cdot R^{\text{pixel}}(\text{blue})\right)}{\ln\left(q \cdot R^{\text{pixel}}(\text{green})\right)} < t \cdot \left(\frac{1}{m} \cdot \sum_{j=1}^{m} \frac{\ln\left(q \cdot R_j^{\text{pixel}}(\text{blue})\right)}{\ln\left(q \cdot R_j^{\text{pixel}}(\text{green})\right)}\right)$$

(7)

where $R_j^{\text{pixel}}(\text{blue})$ and $R_j^{\text{pixel}}(\text{green})$ are the spectral reflectance calculated from the pixel DN values at the blue and green bands of the multispectral imagery acquired with the jth group of view angles (m groups of view angles in total), respectively; q is a fixed constant for all cases, and its value is given to ensure that the logarithm is positive under any condition; and t is a tunable parameter given by users, which controls the degree to which the logarithmic blue/green ratio is less than the average ratio. t took a value of 0.96 in this research, meaning that the multispectral data of a pixel are not used for depth determination when the logarithmic blue/green ratio is less than 96% of the average ratio. The larger the t-value is, the more nonoptimal pixels are excluded. If the t-value is too large, excessive exclusion may happen. An empirical interval for t is (0.9, 1.0) taking into consideration both the range of the ratio and the desired exclusion results.

The criterion uses the blue and green bands because blue and green light has good water penetration characteristics. Different wavelengths of light penetrate water to varying degrees [7]. In clear water, blue light (440–540 nm) can penetrate down to 30 m depth, green light (500–600 nm) to 15 m, red light (600–700 nm) to 5 m, and NIR (700–800 nm) to 0.5 m [48]. Although the depth of light penetration in turbid water reduces with the increase of turbidity [7], blue light still has the strongest penetration ability in turbid water, and green light the second strongest one [49]. Therefore, blue and green lights are optimum and suboptimum spectral bands for bathymetry, respectively.

The ratio of the logarithm-transformed reflectances is used due to its positive correlation with the corresponding depth. This ratio is more sensitive to depth than to bottom reflectance [7] and can approximate depth independently of bottom albedo [5]. Increasing depth will induce a faster decrease in the spectral reflectance at the green band than that at the blue band [7], further leading to the higher logarithmic blue/green ratio. In bathymetric retrieval, a higher logarithmic blue/green ratio will give a larger estimated depth value, and a lower logarithmic blue/green ratio will give a smaller estimated depth value.

Nonoptimal images often have higher environmental noise and/or higher atmospheric path scattering. Generally, depths are underestimated from nonoptimal images compared with the optimal or near-optimal images [34]. Depth underestimation comes from an underestimated logarithmic blue/green ratio. To rule out nonoptimal pixels that result in depth underestimation, pixels with underestimated logarithmic blue/green ratios must be excluded from bathymetric retrieval. The criterion is designed to rule out nonoptimal pixels that result in depth underestimation. That is why only those pixels are filtered for which the logarithmic blue/green ratio is less than the average ratio.

A pixel in the individual image is a nonoptimal one when it satisfies the inequality (7). Nonoptimal pixels are not allowed to
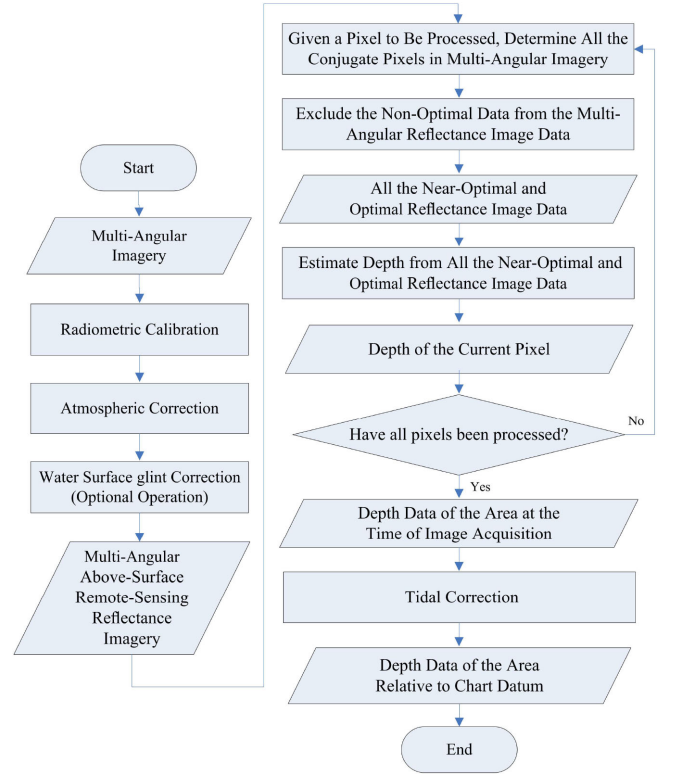

Fig. 1. Flowchart of selective bathymetric retrieval.

participate in bathymetric retrieval in order to prevent them from diminishing the contribution of other conjugate pixels to the retrieval. For simplicity, bathymetric retrieval selectively using multiangular image data is referred to as a selective one. The process of selective bathymetric retrieval is illustrated in Fig. 1.

C. Image Preprocessing, Tidal Correction, and Accuracy Assessment

In physics-based bathymetry, image preprocessing typically includes radiometric calibration, atmospheric correction, and sun glint removal. Radiometric calibration and atmospheric correction are necessary for the accurate derivation of water-leaving reflectance from pixel DN values of satellite imagery. Sun glint removal is an optional operation, which is performed only when the imagery has sun glint.

Radiometric calibration converts image pixel DN values to the reflectance of objects at the sensor. The universal algorithm [19] plus the specific sensor calibration data were used for radiometric calibration. Atmospheric correction is the process to retrieve the reflectance at the Earth's surface from remotely sensed imagery by removing the atmospheric effects (scattering and absorption). The 6S (Second Simulation of Satellite Signal in the Solar Spectrum) method [50] was used for atmospheric correction because it has an advanced radiative transfer code designed to simulate the reflection of solar radiation by a coupled atmosphere-surface system for a wide range of atmospheric, spectral, and geometrical conditions [19].

Sun glint is a limiting factor for optical RS bathymetry. The satellite imagery of lakes or seas sometimes contains solar
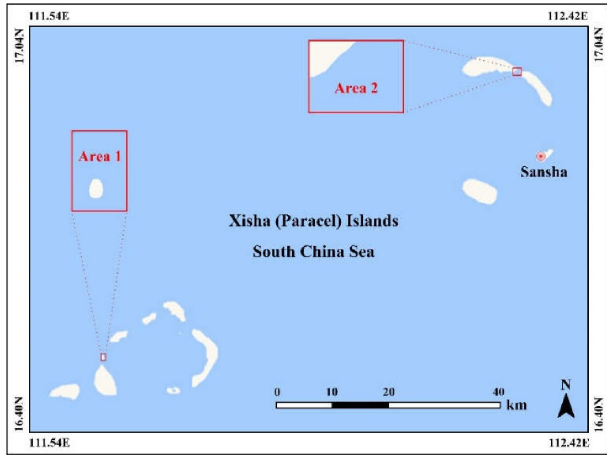
Fig. 2.   Location of the two validation areas in the Xisha (Paracel) Islands in the South China Sea.

glint so that underwater features (including bottom features) are confused or even invisible. Deglinting removes sun glint from satellite imagery. Hedley's method of deglinting [51] is robust, does not require masking, and can be implemented very easily. So, it was offered to remove sun glint on satellite multispectral imagery if needed.

Tidal correction is also necessary for sea bathymetry. In this research, image acquisition time was known, and therefore, the height difference between the tidal state and the highest tide could be derived from the tabulated values. The height difference was then used for the tidal correction of image-based bathymetric data [52].

This article uses the RMSE and the output of regression analysis to assess bathymetric retrieval results derived from satellite imagery. The output of regression analysis includes the coefficient of determination for the linear regression model (denoted by R^2, $R^2 = r^2$, where r is the correlation) as well as the slope and intercept of the regression line [9], [19], [20], [52]. The RMSE is a measure of the differences between the derived depths and the validation depths. In general, a lower RMSE is better than a higher one. The output of regression analysis represents the fitness degree (i.e., degree of correlation) between the derived depths and the validation depths. In general, an R^2 value closer to 1 (R^2 ranges from 0 to 1) and a slope closer to 1 with a smaller intercept indicate a better fit to the validation depths.

This article also uses the relative bathymetric error (RBE) to show the error at a certain position. The RBE for a given validation point is defined as follows:

$$\text{RBE} = \left(\frac{h - h'}{h'}\right) \times 100\% \qquad (8)$$

where h' is the validation depth, and h is the derived depth.

D. Validation Areas and Data

Two typical validation areas (referred to as Areas 1 and 2, see Fig. 2) were selected for our project exploring optical satellite RS bathymetry in the Xisha (Paracel) Islands within the South China Sea. Area 1 was located in the Yongle (Crescent) Group of the Xisha Islands, which included an oceanic island and its immediate clear-water areas. The bottom substrate around the island was sand and that in other areas was sand, mud, and coral reef [52]–[54]. Area 2 was located between the Tree Island and the Qilianyu subgroup in the Xuande (Amphitrite) Group of the Xisha Islands, where the water is clear and the bottom substrate was sand (upper-left part) and coral reef (lower and right part) [52]–[54].

As mentioned in Section I, the stereopairs provided by WorldView-2 contain ideal two-angle multispectral images for bathymetry. We bought two WorldView-2 eight-band multispectral stereopairs (referred to as Scene 1 and Scene 2) for this research. Scene 1 included the two-angle images of Area 1 [see Fig. 3(a)–(c)]. The forward image of Area 1 [see Fig. 3(a)] had acute sun glint, while the backward image [see Fig. 3(c)] did not have sun glint. Fig. 3(b) shows the forward image after sun glint correction. Scene 2 included the two-angle images of Area 2 [see Fig. 4(a) and (b)], both of which were glint free. The NIR 1 and NIR 2 bands of the WorldView-2 multispectral images had nearly no information about the water column and bottom. Therefore, the six bands except NIR 1 and NIR 2 were used for bathymetric retrieval.

Table I presents the related information about Scene 1 and Scene 2. The acquisition time difference between the two images in each area was not more than 2 min. In such a short period of time, the bottom and water column could be considered unchanged. Note that the optimal time difference depends on the variability of the water body, and the multiangular images acquired during the period of the satellite flying over the target area in the same pass can generally be used to infer bathymetry.

All the validation data in the two study areas were collected by bathymetric SONAR (SDE-28S+ [53]) in May 2017, which are shown in Figs. 3(d) and (e), and 4(c) and (d). The bathymetric accuracy of SDE-28S+ is 1 cm $\pm$ 0.1%H (H is the water depth) [52], [55]; and the horizontal accuracy depends on the GPS used together. There were 2054 and 997 validation points in Areas 1 and 2, respectively. Figs. 3(e) and 4(d) show that the validation points in Area 1 were much denser than those in Area 2.

III. Results

In this research, the two multispectral images of each area were used for bathymetric retrieval. Three image data options were available for every pixel in selective bathymetric retrieval: the pixel data of one single image, the pixel data of the other single image, and the pixel data of both images. The selective bathymetric retrieval method identified the best one from the three image data options for bathymetric retrieval. The image data used at different pixel locations might come from the different single images. The image dataset used at all pixel locations after the exclusion of nonoptimal pixels is referred to as "selective image data," which are a part of the multiangular imagery but do not include its nonoptimal pixels.

A. Results of Area 1

Selective bathymetric retrieval was first performed on the two-angle images of Area 1. A digital depth model (DDM) [see
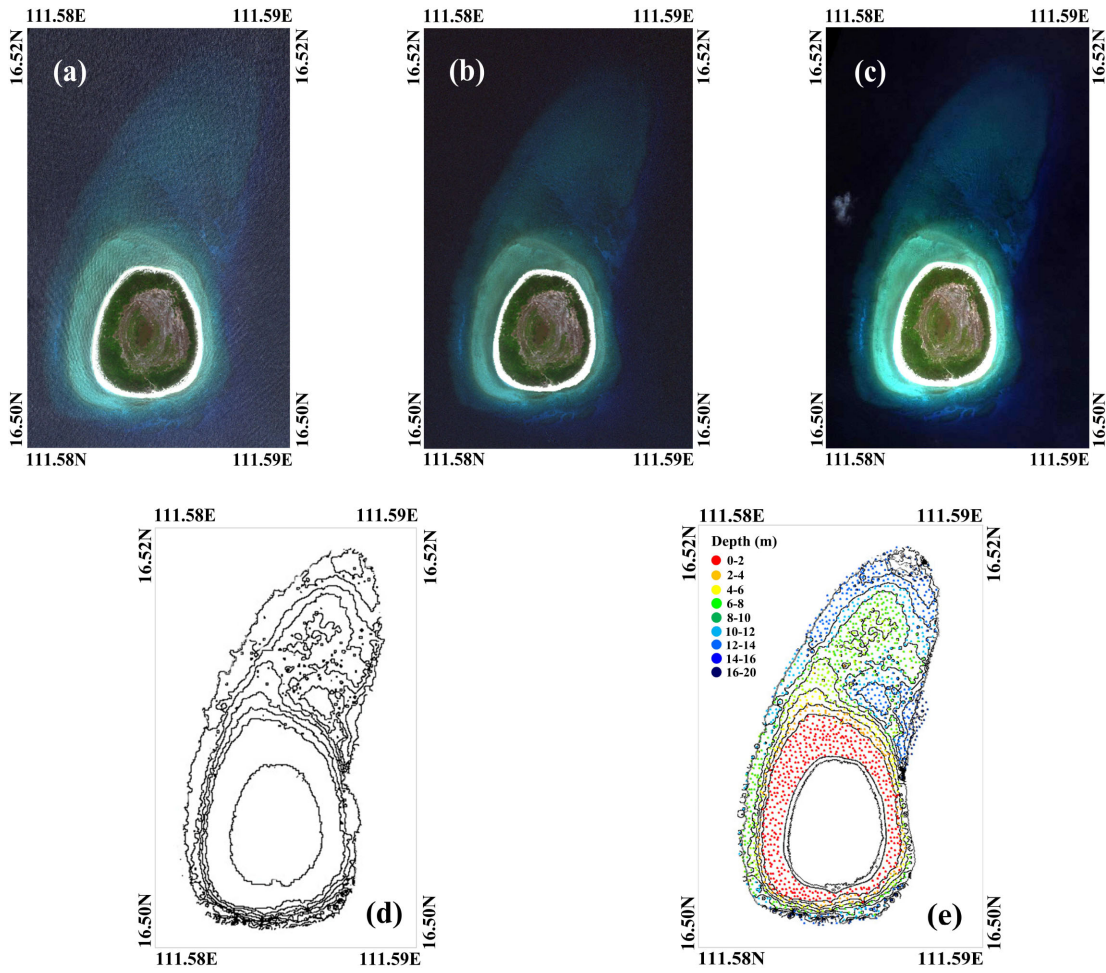
Fig. 3. WorldView-2 imagery and SONAR validation data for Area 1. (a) Forward image (before sun glint correction). (b) Forward image (after sun glint correction). (c) Backward image (glint free). (d) Validation data shown with depth contour lines. (e) Validation data shown with depth contour lines plus validation points. Each image was composed by mapping the red, green, and blue bands of the multispectral image to the RGB space.

TABLE I
RELATED INFORMATION ON SCENE 1 AND SCENE 2 (ANGLE IN DEGREE, TIME IN UTC)

	Scene 1		Scene 2	
	Forward Image	**Backward Image**	**Forward Image**	**Backward Image**
Acquisition Time	2015-11-03T04:16:38	2015-11-03T04:18:09	2017-8-4T3:20:36	2017-8-4T3:22:35
Sun Zenith Angle	19.7	19.4	31.6	31.4
Sun Azimuth Angle	124.0	124.5	128.2	128.7
Sun Elevation Angle	70.3	70.6	58.4	58.6
Satellite Zenith Angle	15.5	36.3	27.6	33.3
Satellite Azimuth Angle	301.4	200.0	67.4	150.5
Satellite Elevation Angle	84.5	53.7	62.4	56.7
In-Track View Angle	2.0	-31.1	12.3	-22.6
Cross-Track View Angle	-4.5	-6.8	21.3	18.9
Off-Nadir View Angle	4.9	31.8	24.5	29.2
Water Surface Condition	Severe Sun Glint	Glint Free	Glint Free	Glint Free
Spatial Resolution	1.84 m at nadir		1.84 m at nadir	
Areas Included	Area 1		Area 2	

Note: A positive in-track view angle indicates the sensor is looking forward and negative looking backward. A positive cross-track view angle indicates the sensor is looking to the right, and negative looking to the left. Each angle value is the mean angle value of the whole image.
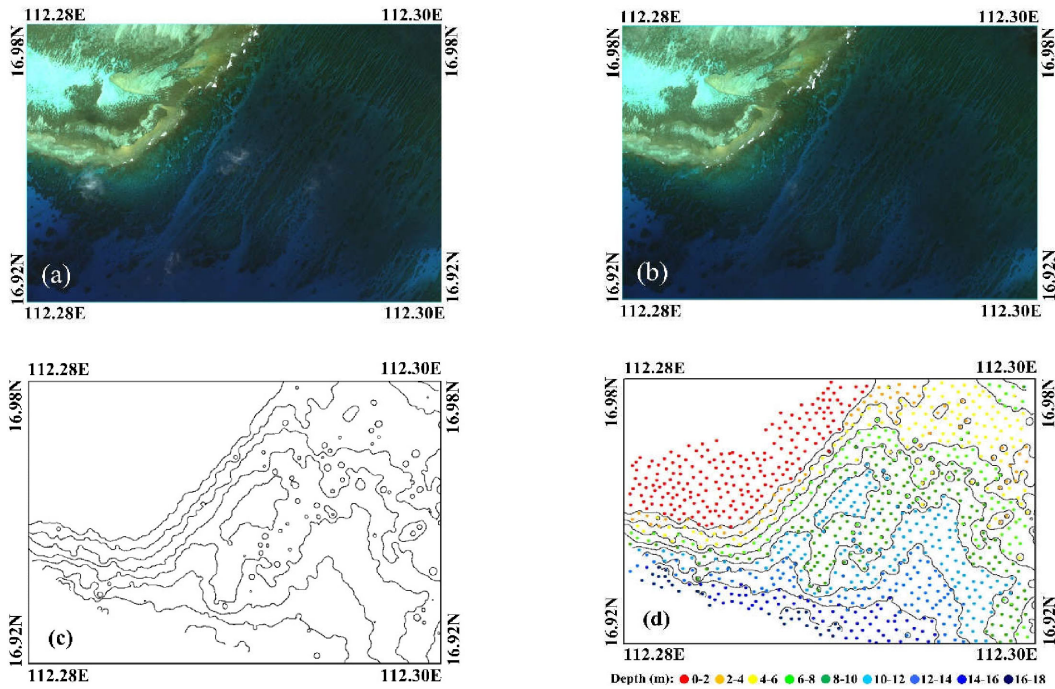
Fig. 4. WorldView-2 imagery and SONAR validation data for Area 2. (a) Forward image. (b) Backward image. (c) Validation data shown with depth contour lines. (d) Validation data shown with depth contour lines plus validation points. Each image was composed by mapping the red, green, and blue bands of the multispectral image to the RGB space.
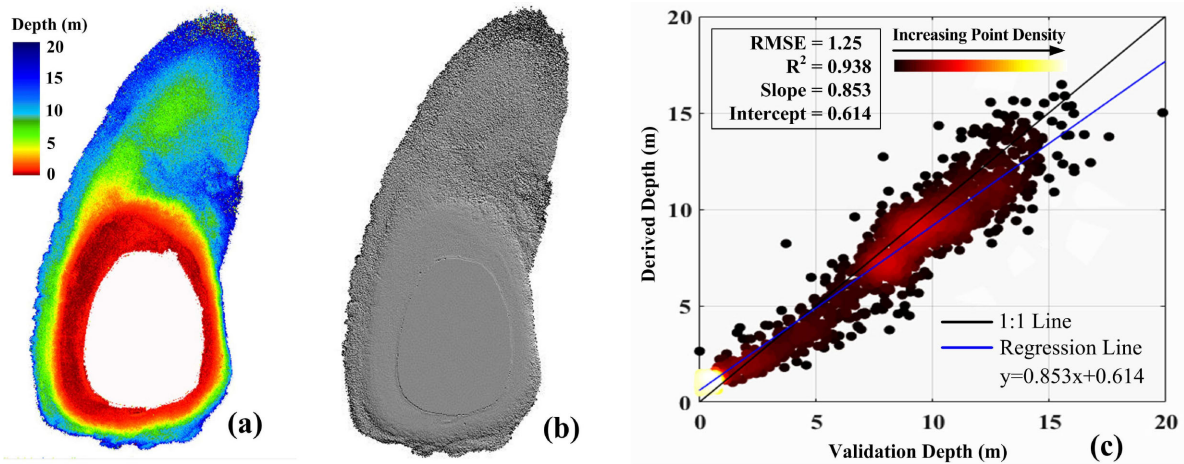

Fig. 5. Bathymetric retrieval results derived from the selective image data of Area 1 (i.e., results derived by the selective bathymetric retrieval method). (a) Color-coded DDM (white color indicates a data void area or the area above the water surface). (b) Shaded DSM. (c) Scatterplot.

Fig. 5(a)] and a digital surface model (DSM) [see Fig. 5(b)] were derived from the selective image data of Area 1. The RMSE of the derived DDM was then calculated by comparing with the validation data. The derived depths were also plotted versus the validation depths, and linear regression analysis was performed. Fig. 5(c) shows the scatterplot, the regression information, and the accuracy in terms of RMSE. The DSM is used here because it is another visualization of the DDM. The DSM is helpful to know the bottom textures.

For comparison, another group of bathymetric retrieval results in Area 1 was derived from the entirety of the two-angle images

(both images) without the exclusion of nonoptimal image pixel data. This group of results also included the DDM [see Fig. 6(a)], the DSM [see Fig. 6(b)], the scatterplot [see Fig. 6(c)], and the accuracy metrics [i.e., RMSE, R^2, slope, and intercept, as shown in Fig. 6(c)].

From Figs. 5 and 6, the DDM derived from the selective image data had an RMSE of 1.25 m, R^2 of 0.938, the slope of 0.853, and intercept of 0.614 m, while the DDM derived from both images (nonoptimal pixel data were not excluded) had an RMSE of 1.52 m, R^2 of 0.925, the slope of 0.817, and intercept of 0.642 m. The DDM from the selective image data provided
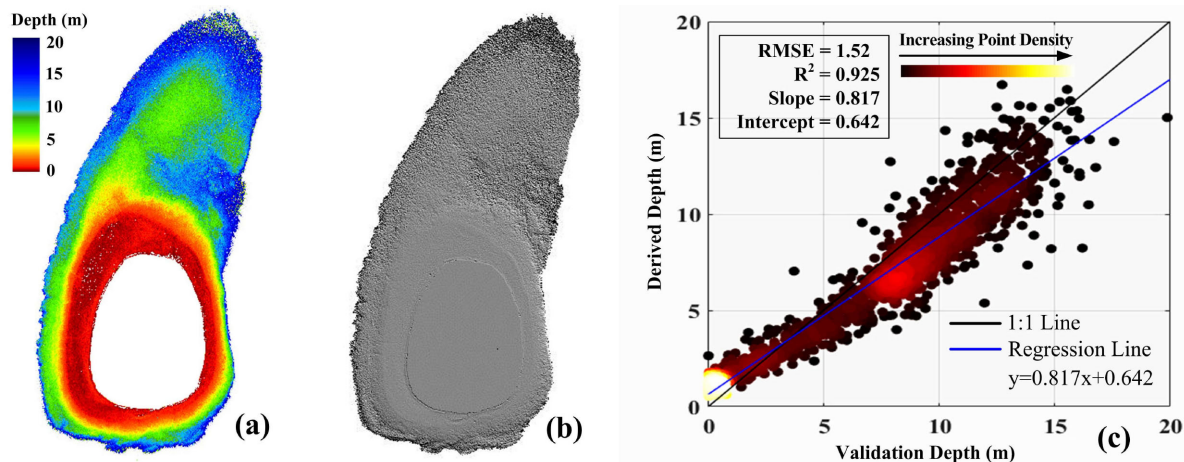
Fig. 6. Bathymetric retrieval results derived from the entirety of the two-angle images (both images) of Area 1. (a) Color-coded DDM (white color indicates a data void area or the area above the water surface). (b) Shaded DSM. (c) Scatterplot. Note that this group of results was derived without the exclusion of nonoptimal image pixel data.
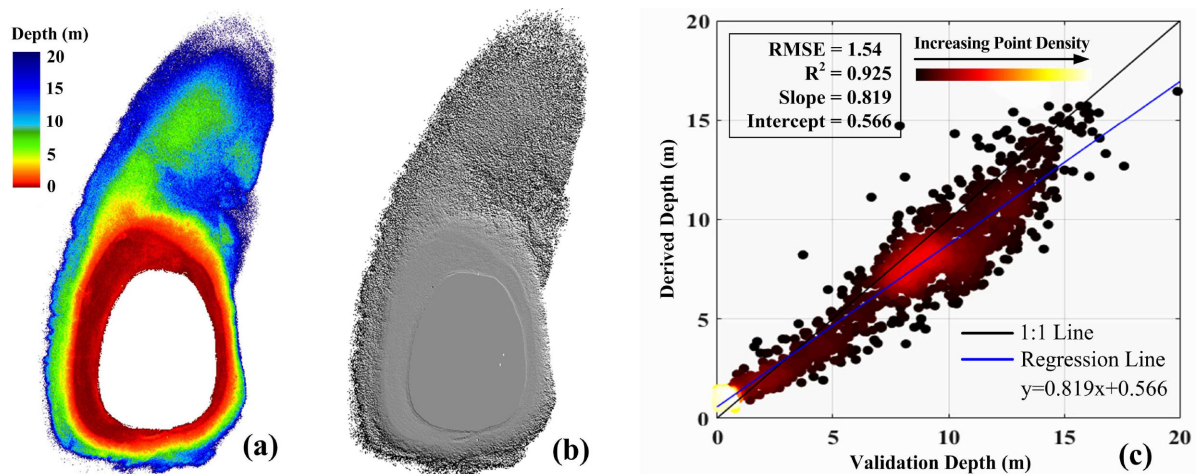

Fig. 7. Bathymetric retrieval results derived from the backward image of Area 1. (a) Color-coded DDM. (b) Shaded DSM. (c) Scatterplot. Note that the derivation of this group of results did not need to exclude nonoptimal image pixel data because only one single image was used.

a better fit to the validation data than the DDM from both images.

To know why the DDM from the selective image data outperformed the DDM from the entirety of the two-angle images, another two groups of bathymetric retrieval results in Area 1, as shown in Figs. 7 and 8, were also derived from the backward image and the forward image, respectively. Every group of bathymetric retrieval results also included the DDM, the DSM, the scatterplot, and the accuracy metrics (i.e., RMSE, R^2, slope, and intercept).

Comparing Figs. 7 and 8 showed that the DDM derived from the backward image had a better fit to the validation data than that from the forward image. From Fig. 8, depths derived from the forward image were, overall, underestimated at the depth range of about 4–18 m; the underestimation became severer with increasing depths. This indicated that many nonoptimal pixels existed in the forward image. Those nonoptimal pixels

further caused that the result derived from the entirety of the two-angle images was worse than that from the selective image data.

To examine whether the excluded image data came mainly from nonoptimal images, we also recorded which image data were actually used at every pixel location in selective bathymetric retrieval. Fig. 9 shows the image data used in the derivation of the DDM [see Fig. 5(a)] from the selective image data. In the red areas, both the forward and backward images were used for bathymetric retrieval (i.e., neither of them was excluded from bathymetric retrieval). In the green areas, only the backward image was used (i.e., the forward image was excluded from bathymetric retrieval). In the blue areas, only the forward image was used (i.e., the backward image was excluded from bathymetric retrieval). From Fig. 9, most of the excluded pixels came from the forward image from which the depths were generally underestimated.
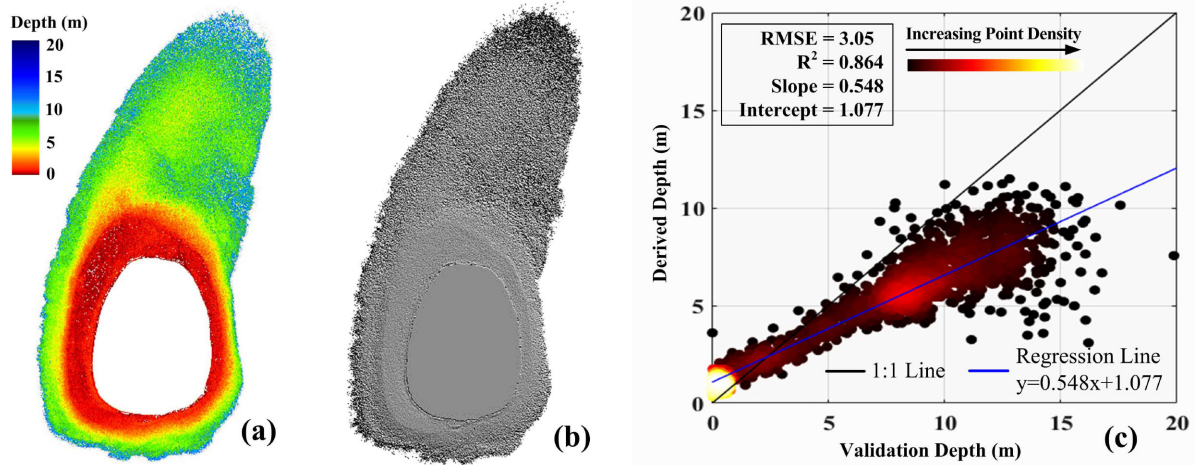
Fig. 8. Bathymetric retrieval results derived from the forward image of Area 1. (a) Color-coded DDM. (b) Shaded DSM. (c) Scatterplot. Note that the derivation of this group of results did not need to exclude nonoptimal image pixel data because only one single image was used.
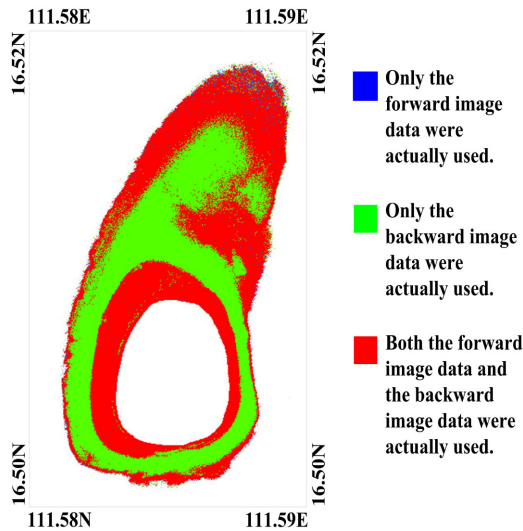

Fig. 9. Image data used at different pixel locations in selective bathymetric retrieval. The blue color at a pixel indicates that the forward image pixel data were actually used for bathymetric retrieval. The green color at a pixel indicates that the backward image pixel data were actually used. The red color at a pixel indicates that the forward and backward image pixel data (i.e., pixel data of both images) were actually used.

B. Results of Area 2

Similarly, four groups of bathymetric retrieval results in Area 2 were derived from the forward image, the backward image, the forward and backward images (i.e., both images), and the selective image data, respectively. Every group of bathymetric retrieval results included the DDM, the DSM, the scatterplot, and their accuracies (including RMSE, R^2, slope, and intercept). Figs. 10 –13 show those four groups of results. We also recorded which image data were actually used at every pixel location in selective bathymetric retrieval in Area 2. Fig. 14 shows the image data used in the derivation of the DDM [see Fig. 13(a)] from the selective image data.

Table II summarizes the accuracies of the four DDMs in Area 2. The DDM of the selective image data had the best fit to the validation data. The backward image followed with the second best fit. The forward and backward images (both images) offered the third best fit. The forward image provided the worst fit. The fit offered by the selective image data was not only better than that provided by every single image but also better than that by both images (i.e., the entirety of both images, including nonoptimal pixels). In other words, the proposed method gave a DDM closest to the validation data. Comparing the scatterplots in Figs. 10(c)– 13(c) also shows such a conclusion.

The DDM [see Fig. 13(a)] derived from the selective image data was based on two-angle images (two images), while both DDMs [see Figs. 10(a) and 11(a)] derived from the forward image and from the backward image were based on one single image. As expected, the DDM derived from the selective image data had a better fit to the validation data than both from the forward image and from the backward image due to a greater number of observations.

The DDM [see Fig. 12(a)] derived from both images was also based on two-angle images (two images). However, the RMSE of the DDM [see Fig. 13(a)] derived from the selective image data was still 0.62 m smaller than that from both images due to the exclusion of nonoptimal pixel data. In other words, the exclusion of nonoptimal image data resulted in a decrease of 0.62 m RMSE.

Unexpectedly, the RMSE of the DDM derived from the backward image was smaller than that from both images. The reason is that in the derivation of the DDM using the forward and backward images, the advantages of the backward image were counteracted and overwhelmed by the disadvantages of the forward image. It follows that the bathymetric retrieval results derived from the whole multiangular imagery are not necessarily better than those from a part of all the single images when nonoptimal pixels existed in some single images. That is why the exclusion of nonoptimal image data is necessary for multiangular imagery-based bathymetric retrieval.
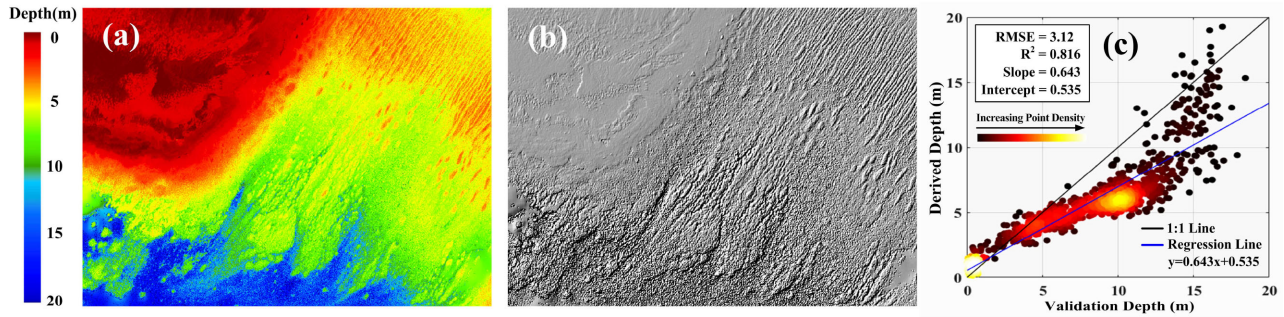
Fig. 10. Bathymetric retrieval results derived from the forward image of Area 2. (a) Color-coded DDM. (b) Shaded DSM. (c) Scatterplot. Note that the derivation of this group of results did not need to exclude nonoptimal image pixel data because only one single image was used.
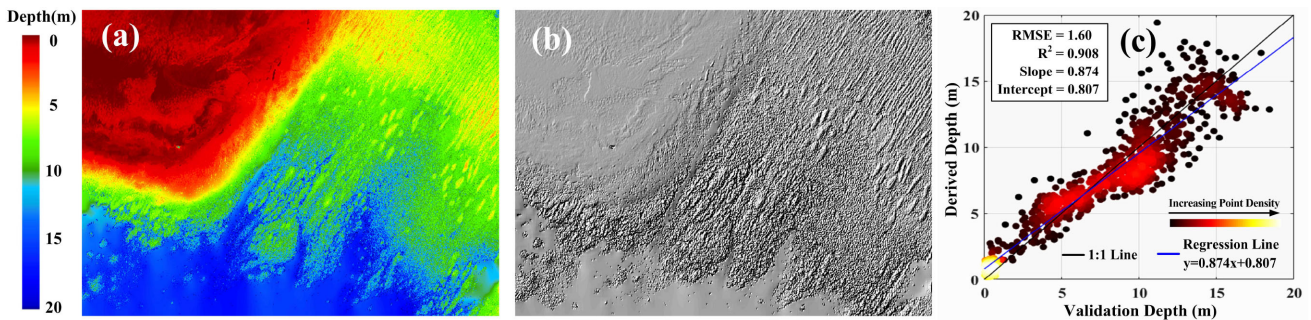

Fig. 11. Bathymetric retrieval results derived from the backward image of Area 2. (a) Color-coded DDM. (b) Shaded DSM. (c) Scatterplot. Note that the derivation of this group of results did not need to exclude nonoptimal image pixel data because only one single image was used.
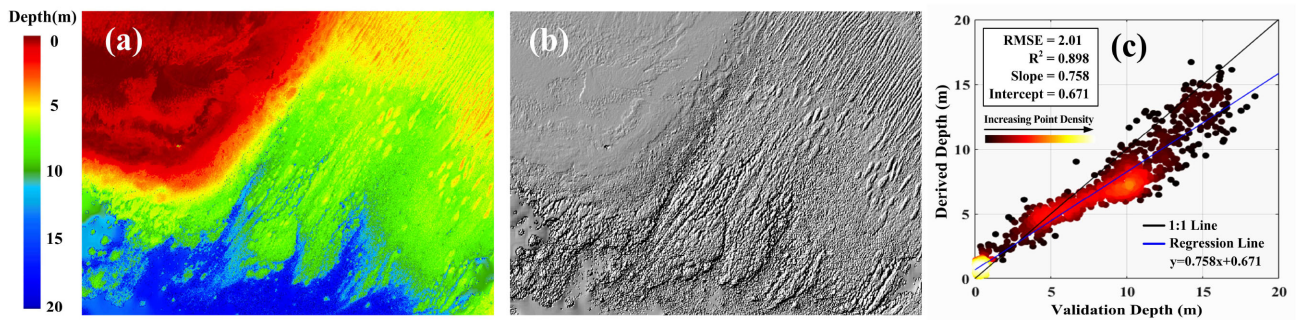

Fig. 12. Bathymetric retrieval results derived from the forward and backward images (i.e., both images) of Area 2. (a) Color-coded DDM. (b) Shaded DSM. (c) Scatterplot. Note that this group of results was derived without the exclusion of nonoptimal image pixel data.

The RMSE of the DDM derived from the forward image was almost twice that from the backward image, implying that many nonoptimal image pixels existed in the forward image. Fig. 10(c) shows that the scatter points deviate nonlinearly from the 1:1 line in deeper water areas (within the depth range of about 6–18 m), and the depths were generally underestimated in those areas. That is why almost all the excluded pixel data in the selective bathymetric retrieval came from the corresponding areas of the forward image (see Fig. 14).

The spatial distribution of RBEs is helpful to know where bathymetric retrieval improved and how many of bathymetric retrieval results from different image data sources changed.

To observe and analyze the spatial distribution of bathymetric retrieval errors as well as its variation among different results, we calculated RBEs of the four DDMs in Area 2 at every validation point and displayed them onto the forward/backward image using specific color symbols representing different RBEs.

Fig. 15(a) and (b) shows the RBEs of DDMs derived from the forward image and from the backward image, respectively. Fig. 15(a) had more validation points that were depth underestimated, compared with Fig. 15(b). The validation points with $|RBE| \geq 20\%$ (i.e., red points) on Fig. 15(b) were much less than those on Fig. 15(a), but the validation points with $|RBE| < 20\%$ (i.e., green and yellow points) on Fig. 15(b) were much
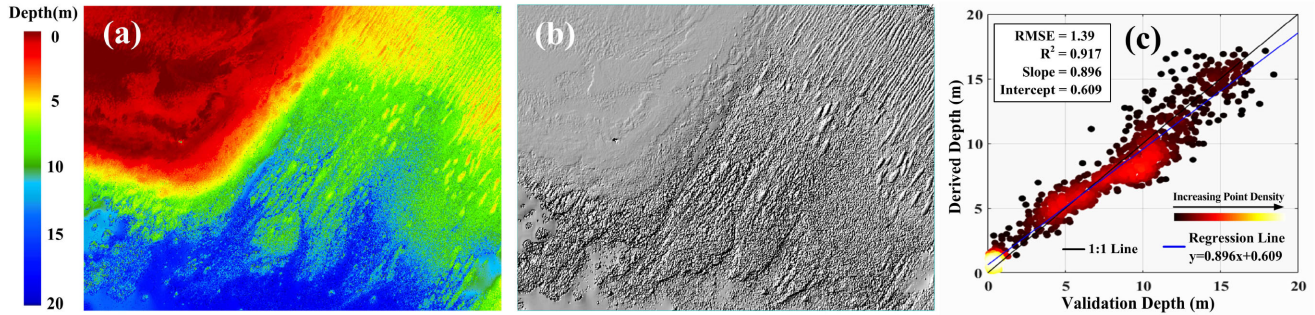
Fig. 13. Bathymetric retrieval results derived from the selective image data of Area 2 (i.e., results derived by the selective bathymetric retrieval method). (a) Color-coded DDM. (b) Shaded DSM. (c) Scatterplot.

TABLE II
BATHYMETRIC RETRIEVAL ACCURACIES FOR THE DDMs IN AREA 2 (RMSE AND INTERCEPT IN METERS, R^2, AND SLOPE ARE DIMENSIONLESS)

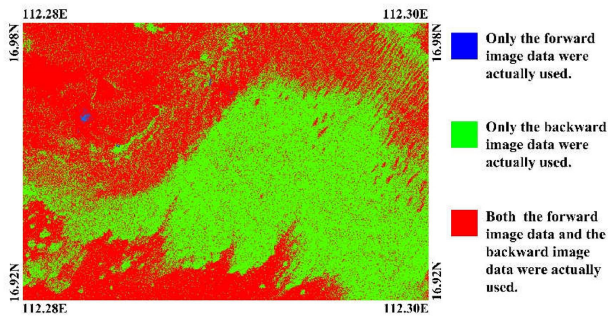|	RMSE	R^2	Slope	Intercept
Forward Image	3.12	0.816	0.643	0.535
Backward Image	1.60	0.908	0.874	0.807
Both Images	2.01	0.898	0.758	0.671
Selective Image Data	1.39	0.917	0.896	0.609

Fig. 14. Image data used at different pixel locations in selective bathymetric retrieval. The blue color at a pixel indicates that the forward image pixel data were actually used for bathymetric retrieval. The green color at a pixel indicates that the backward image pixel data were actually used. The red color at a pixel indicates that the forward and backward image pixel data (i.e., pixel data of both images) were actually used.

more than those on Fig. 15(a). The comparison showed that the backward image outperformed the forward image in bathymetric performance.

Fig. 15(c) shows RBEs of the DDM derived from the forward and backward images (both images). The validation points with |RBE| ≥ 20% (i.e., red points) on Fig. 15(c) were much less than those on Fig. 15(a) but still more than those on Fig. 15(b). A part of RBEs on Fig. 15(c) is better than those on Fig. 15(a) due to the positive effect of the backward image but still worse than those on Fig. 15(b) due to the negative effect of nonoptimal pixels in the forward image. Comparing Fig. 15(a)–(c) showed that the result at every validation point, derived from the forward and backward images, combined the bathymetric information of all the conjugate pixels, including that of the nonoptimal and optimal pixels.

Fig. 15(d) shows the RBEs of the DDM derived from selective image data. Compared with Fig. 15(c), the validation

points with |RBE| ≥ 20% (i.e., red points) on Fig. 15(d) decreased significantly, but the validation points with |RBE| < 20% (i.e., green and yellow points) on Fig. 15(d) increased significantly. The underestimated validation points on Fig. 15(d) were also less than those on Fig. 15(c). This comparison showed that the selective image data outperformed the forward and backward images (both images) in bathymetric performance by excluding nonoptimal pixels in every single image. Careful comparison among Fig. 15(a)–(d) showed that the result at every validation point, derived from the selective image data, used the bathymetric information of the conjugate pixels selectively, using their advantages and avoiding their disadvantages.

RBEs at a few validation points in the upper-right corner of Fig. 15(d) were still larger than those of Fig. 15(a) and (c). Those validation points were situated in relatively shallow-water areas [about 2–4 m deep, see Fig. 4(d)] where suspended particles probably existed. Those suspended particles could lead to the failure to exclude nonoptimal pixels at those points because the exclusion criterion is based on the penetration ability of light in water.

IV. DISCUSSION

In the experiments, we found that many nonoptimal pixels existed in the forward images of both areas, the nonoptimal pixels resulted in depth underestimation, and bathymetric retrieval results were improved by excluding nonoptimal image data in selective bathymetric retrieval. This section analyzes what factors caused nonoptimal pixels and why the proposed method gave the desired bathymetric retrieval results.

A. Discussion About Area 1

One of the greatest confounding factors limiting the quality and accuracy of remotely sensed data from water bodies is sun
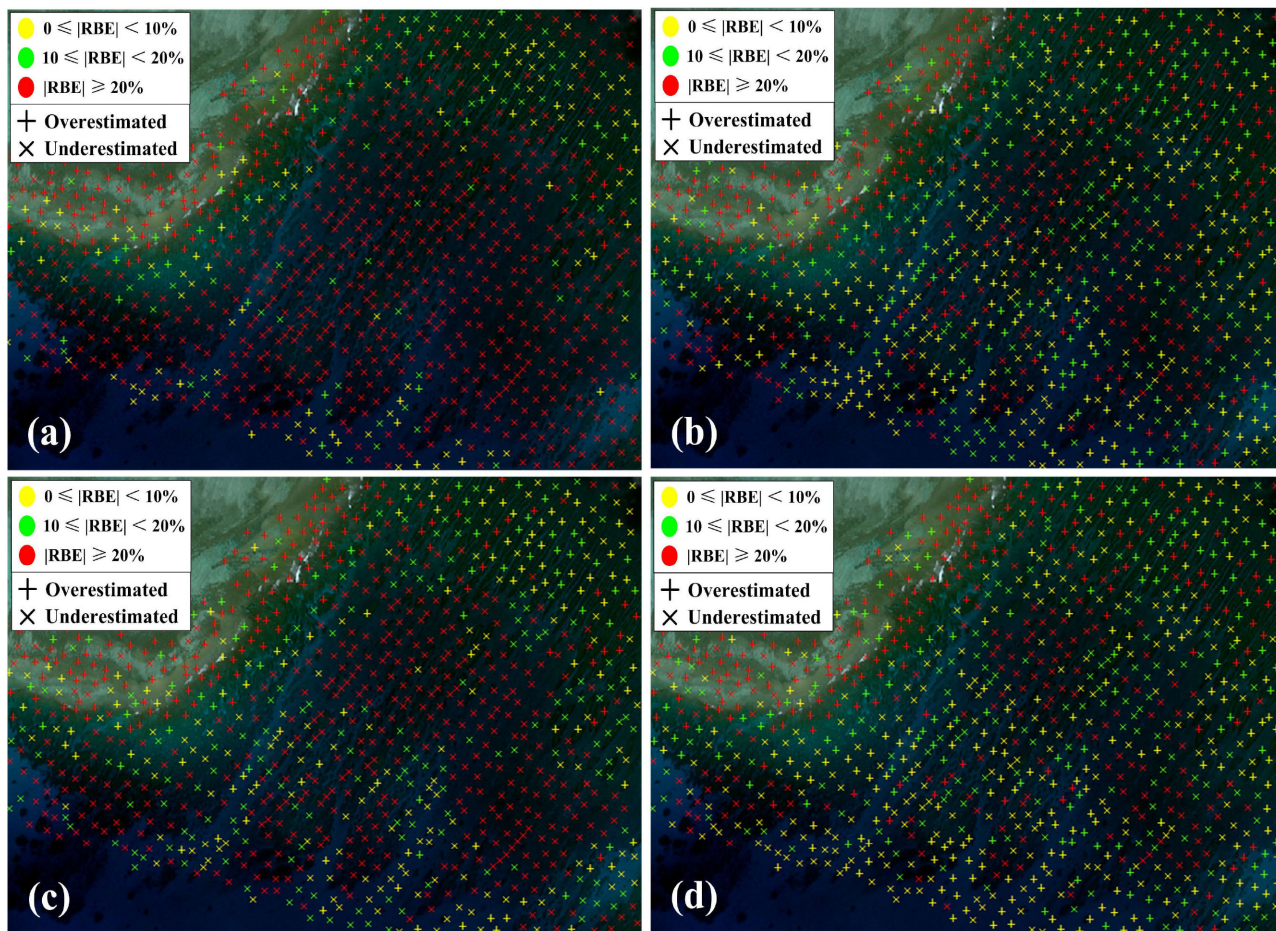
Fig. 15. RBEs at all the validation points for four DDMs derived from (a) forward image, (b) backward image, (c) forward and backward images (both images), and (d) selective image data. Red symbols indicate that the absolute RBEs are greater than or equal to 20%. Green symbols indicate the absolute RBEs are in the 10%–20% interval. Yellow symbols indicate the absolute RBEs are less than 10%. Symbol "+" indicates the error is positive, i.e., the depth is overestimated. Symbol "×" indicates the error is negative, i.e., the depth is underestimated.

glint, which in high-resolution imagery will lead to errors as large as 30% in the measurement of water depth [31]. The effect of sun glint on bathymetric retrieval is usually dominant over that of other factors, such as sun elevation and azimuth, satellite sensor pointing, and sun-sensor-target geometry.

Existing glint correction methods are based on the assumption that the water-leaving radiance at the NIR band is negligible and, therefore, any NIR signal remaining after the atmospheric correction must be due to sun glint [31], [51]. The spectrum for a deep water part of an image is used to establish the relationship between the NIR and glint radiances, and then used for the glint correction of the entire image [31], [51]. That assumption is valid for optically deep water areas where the bottom influence is negligible. However, it is not valid for optically shallow-water areas, especially for very shallow (<2 m) or turbid water areas. Sun glint in high-spatial-resolution images cannot be thoroughly eliminated by existing glint correction methods. Glint radiance remaining after sun glint correction always exists and varies with the depth. The smaller the depth value is, the greater the residual glint radiance is. Glint correction will widen the bathymetric performance difference not only between the shallow-water part

of an image and the deep water part but also between images acquired with different view angles.

The exclusion of nonoptimal pixels happens only in areas where different individuals of multiangular imagery have large differences in bathymetric performance. In Area 1, the forward image [see Fig. 3(a)] had heavy sun glint, while the backward image [see Fig. 3(c)] did not have sun glint. Although sun glint correction was performed on the forward image, a part of the glint radiance remained in optically shallow-water areas around the island on the image. Owing to the reasons mentioned above, glint correction increased the likelihood of pixels in the relatively shallow-water areas (not including very shallow (<2 m) turbid areas adjacent to the island) to be excluded. Comparing Figs. 3(e) and 9 also showed that the exclusion of nonoptimal image data in selective bathymetric retrieval happened mainly in the area of about 2–10 m deep rather than in the area of 10–18 m deep. This is consistent with the above analysis.

The effect of severe sun glint in an image, on bathymetric retrieval, cannot be thoroughly eliminated during image pre-processing. It must be taken into consideration in bathymetric

retrieval algorithms. This is one of the problems solved by the proposed method.

From Figs. 5(a)–8(a), we also noticed that there were some void values in the deep water part of the DDMs. The void points of the DDMs derived from the selective image data were not only less than those of the entire two-angle images but also less than those of the forward or backward image. The decrease in void points resulted from the exclusion of nonoptimal image data or the use of two-angle observations. The six bands (not including NIR 1 and NIR 2) of WorldView-2 multispectral images are superficially adequate for solving the six-parameter bio-optical RTM. However, those six bands are still not enough for solving the bathymetric model in relatively deep (about 15–20 m) areas because the RedEdge and red bands have nearly no information about the water column and bottom at that depth range. Using multispectral imagery acquired with three or more different view angles during the same satellite pass can perhaps improve the bathymetric results obtained using two-angle images. Unfortunately, this kind of image product is not yet easily available.

B. Discussion About Area 2

In Area 2, the forward image [see Fig. 4(a)] and the backward image [see Fig. 4(b)] did not have sun glint. However, the backward image still performed better in bathymetric retrieval than the forward image, and the exclusion of nonoptimal image data in selective bathymetric retrieval happened mainly in the green areas in Fig. 14. Which of the following factors caused the phenomena: sun illumination direction, sensor pointing, sun-sensor-target geometry, bottom surface properties, or some combination?

As mentioned in Table I, the forward and backward images had similar sun elevation and azimuth angles but different satellite sensor pointing angles. The quality difference of both images resulted mainly from their different off-nadir view angles and sun-sensor-target geometry. Larger off-nadir view angles result in higher path scattering due to a longer path length through the atmosphere [2]. Although the mean off-nadir view angle of the backward image (29.2°) was a little bigger than that of the forward image (24.5°), the resultant image radiometric quality difference had been eliminated by the atmospheric correction in image preprocessing.

The bidirectional reflectance function of a target, measured by a sensor, is strongly dependent on the geometric relationship of illumination and observation at the time of image acquisition [56]. Optimal sun-sensor-target geometry over water includes the solar zenith angles of 30°–60° and the sensor azimuth angles of 0°–180° with respect to the solar azimuth [57]. From Table I, both of the forward and backward images were acquired with optimal solar zenith angles (31.6° and 31.4°). However, the forward image was acquired using a mean sensor azimuth angle of 60.8° with respect to the solar azimuth, and the backward image was acquired using a mean sensor azimuth angle of 21.8° with respect to the solar azimuth. In terms of sensor azimuth angles, the sun-sensor-target geometry of the backward image was closer to the optimal one than that of the forward image. Accordingly, the image quality of the backward image was better
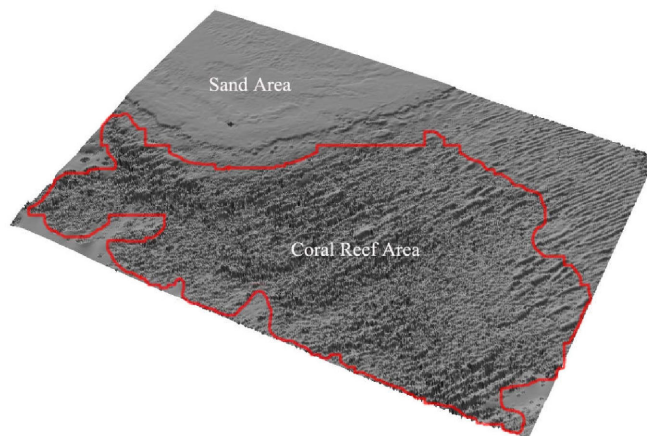

Fig. 16.   Different types of bottom textures appeared in different parts of Area 2. This figure is generated using the DSM derived from the selective image data.

than that of the forward image. This is why the backward image could offer better bathymetric information than the forward image.

The intensity and direction of reflected light from a target are also influenced by the surface texture [58]. The intensity and direction change frequently within a rough area. Satellite sensors can only collect radiation in their viewing direction. From the 3-D DSM in Area 2 (see Fig. 16), the coral reef area had a rough texture, while the sand area had a smooth texture. The quality difference in the coral reef area between the forward image and the backward image was greater than that in the sand area. This explains why the exclusion of nonoptimal image data in selective bathymetric retrieval happened mainly in the coral reef area (see Figs. 14 and 16).

The effect of image quality variation caused by nonoptimal sun-sensor-target geometry and target surface properties, on bathymetric retrieval, cannot be eliminated during image preprocessing. The bathymetric retrieval algorithm itself must take this effect into consideration. Bottom surface texture may vary in different water areas. The resultant effect must be removed pixel-by-pixel rather than image-by-image.

V. CONCLUSION

This article has proposed a selective bathymetric retrieval method to eliminate the negative effect of nonoptimal image data on bathymetric information in multiangular imagery-based bathymetric retrieval. The method can use multiangular image data selectively using their advantages and avoiding their disadvantages. The method can also avoid that bathymetric retrieval results from the entirety of the multiangular images are poorer than those from a part of the individual images. The method has been tested in two areas within the Xisha (Paracel) Islands of the South China Sea using two-angle WorldView-2 multispectral images. The resulting accuracy was 1.25 m in Area 1 and 1.39 m in Area 2. The derived depths of the proposed method (i.e., depths derived from the selective image data) in each area provided a better fit to the validation depths than those from the entirety of the two-angle images. The underestimation of depths

derived from the entirety of both images, caused by nonoptimal image data, was also improved to some extent.

Another SDB method is the through-water photogrammetric method [59], which is also based on stereoimagery. Further work will concentrate on comparing and integrating the proposed method and the established through-water photogrammetric method.

REFERENCES

[1] The Free Dictionary, Bathymetry. Accessed: Mar. 20, 2020. [Online]. Available: https://encyclopedia.thefreedictionary.com/Bathymetry

[2] M. Hodúl, S. Bird, A. Knudby, and R. Chénier, "Satellite derived photogrammetric bathymetry," *ISPRS J. Photogrammetry Remote Sens.*, vol. 142, pp. 268–277, 2018.

[3] R. Chénier, M.-A. Faucher, and R. Ahola, "Satellite-derived bathymetry for improving Canadian hydrographic service charts," *ISPRS Int. J. Geo-Inf.*, vol. 7, no. 8, pp. 306–321, 2018.

[4] S. Jawak, S. S. M. Vadlamani, and A. Luis, "A synoptic review on deriving bathymetry information using remote sensing technologies: Models, methods and comparisons," *Adv. Remote Sens.*, vol. 4, no. 2, pp. 147–162, 2015.

[5] R. P. Stumpf, K. Holderied, and M. Sinclair, "Determination of water depth with high-resolution satellite imagery over variable bottom types," *Limnol. Oceanogr.*, vol. 48, no. 1-part 2, pp. 547–556, 2003.

[6] K. R. Hogrefe, D. J. Wright, and E. J. Hochberg, "Derivation and integration of shallow-water bathymetry: Implications for coastal terrain modeling and subsequent analyses," *Mar. Geodesy*, vol. 31, no. 4, pp. 299–317, 2008.

[7] H. Su, H. Liu, and W. D. Heyman, "Automated derivation of bathymetric information from multi-spectral satellite imagery using a non-linear inversion model," *Mar. Geodesy*, vol. 31, pp. 281–298, 2008.

[8] V. E. Brando, J. M. Anstee, M. Wettle, A. G. Dekker, S. R. Phinn, and C. Roelfsema, "A physics based retrieval and quality assessment of bathymetry from suboptimal hyperspectral data," *Remote Sens. Environ.*, vol. 113, no. 4, pp. 755–770, 2009.

[9] S. Ma, Z. Tao, X. Yang, Y. Yu, X. Zhou, and Z. Li, "Bathymetry retrieval from hyperspectral remote sensing data in optical-shallow water," *IEEE Trans. Geosci. Remote Sens.*, vol. 52, no. 2, pp. 1205–1212, Feb. 2014.

[10] S. M. Hamylton, J. D. Hedley, and R. J. Beaman, "Derivation of high-resolution bathymetry from multispectral satellite imagery: A comparison of empirical and optimisation methods through geographical error analysis," *Remote Sens.*, vol. 7, no. 12, pp. 16257–16273, 2015.

[11] N. M. Said, M. R. Mahmud, and R. C. Hasan, "Satellite-derived bathymetry: Accuracy assessment on depths derivation algorithm for shallow water area," in *Proc. ISPRS - Int. Arch. Photogrammetry, Remote Sens. Spatial Inf. Sci.*, 2017, vol. XLII-4/W5, pp. 159–164.

[12] Y. G. Morel and F. Faveretto, "4SM: A novel self-calibrated algebraic ratio method for satellite-derived bathymetry and water column correction," *Sensors*, vol. 17, no. 7, pp. 1682–1705, 2017.

[13] Z. Lee, K. L. Carder, C. D. Mobley, R. G. Steward, and J. S. Patch, "Hyperspectral remote sensing for shallow waters—2: Deriving bottom depths and water properties by optimization," *Appl. Opt.*, vol. 38, no. 18, pp. 3831–3843, 1999.

[14] C. J. Legleiter and D. A. Roberts, "A forward image model for passive optical remote sensing of river bathymetry," *Remote Sens. Environ.*, vol. 113, no. 5, pp. 1025–1045, 2009.

[15] K. R. L. West, R. C. Olsen, F. A. Kruse, and A. Kim, "Using multi-angle WorldView-2 imagery to determine bathymetry near Oahu, Hawaii," *Proc. SPIE, Int. Soc. Opt. Eng.*, vol. 8743, 2013, Art. no. 874311.

[16] D. R. Lyzenga, "Passive remote sensing techniques for mapping water depth and bottom features," *Appl. Opt.*, vol. 17, no. 3, pp. 379–383, 1978.

[17] D. R. Lyzenga, "Remote sensing of bottom reflectance and water attenuation parameters in shallow water using aircraft and Landsat data," *Int. J. Remote Sens.*, vol. 2, no. 1, pp. 71–82, 1981.

[18] D. R. Lyzenga, "Shallow-water bathymetry using combined LIDAR and passive multispectral scanner data," *Int. J. Remote Sens.*, vol. 6, no. 1, pp. 115–125, 1985.

[19] F. Eugenio, J. Marcello, and J. Martin, "High-resolution maps of bathymetry and benthic habitats in shallow-water environments using multispectral remote sensing imagery," *IEEE Trans. Geosci. Remote Sens.*, vol. 53, no. 7, pp. 3539–3549, Jul. 2015.

[20] J. D. Hedley *et al.*, "Coral reef applications of Sentinel-2: Coverage, characteristics, bathymetry and benthic mapping with comparison to Landsat 8," *Remote Sens. Environ.*, vol. 216, pp. 598–614, 2018.

[21] M. Barbarella, M. Fiani, and C. Zollo, "Assessment of DEM derived from very high-resolution stereo satellite imagery for geomorphometric analysis," *Eur. J. Remote Sens.*, vol. 50, no. 1, pp. 534–549, 2017.

[22] J. D. Hedley, C. M. Roelfsema, S. R. Phinn, and P. J. Mumby, "Environmental and sensor limitations in optical remote sensing of coral reefs: Implications for monitoring and sensor design," *Remote Sens.*, vol. 4, pp. 271–302, 2012.

[23] Satellite Imag. Corp., "Characterization of satellite remote sensing systems." Accessed: Sep. 20, 2019. [Online]. Available: https://www.satimagingcorp.com/services/resources/characterization-of-satellite-remote-sensing-systems/

[24] DigitalGlobe, IKONOS data sheet. Accessed: Sep. 20, 2019. [Online]. Available: http://www.digitalglobe.com/

[25] DigitalGlobe, QuickBird data sheet. Accessed: Sep. 20, 2019. [Online]. Available: https://www.euspaceimaging.com/wp-content/uploads/2018/06/QuickBird-DS-QB-Prod.pdf

[26] GeoEye, GeoEye-1 fact sheet. Accessed: Sep. 20, 2019. [Online]. Available: http://www.geoeye.com/

[27] Astrium, Spot_6_7_technical_sheet. Accessed: Sep. 20, 2019. [Online]. Available: https://directory.eoportal.org/web/eoportal/satellite-missions/s/spot-6-7

[28] DigitalGlobe, "WorldView-2/3/4 satellite sensor specifications." Accessed: Sep. 20, 2019. [Online]. Available: https://www.satimagingcorp.com/satellite-sensors/worldview-2/

[29] R. Huang, K. Yu, Y. Wang, J. Wang, L. Mu, and W. Wang, "Bathymetry of the coral reefs of Weizhou island based on multispectral satellite images," *Remote Sens.*, vol. 9, no. 7, pp. 750–774, 2017.

[30] Z. Lee, A. Weidemann, and R. Arnone, "Combined effect of reduced band number and increased bandwidth on shallow water remote sensing: The case of WorldView 2," *IEEE Trans. Geosci. Remote Sens.*, vol. 51, no. 5, pp. 2577–2586, May 2013.

[31] S. Kay, J. D. Hedley, and S. Lavender, "Sun glint correction of high and low spatial resolution images of aquatic scenes: A review of methods for visible and near-infrared wavelengths," *Remote Sens.*, vol. 1, no. 4, pp. 697–730, 2009.

[32] J. A. Goodman, Z. Lee, and S. L. Ustin, "Influence of atmospheric and sea-surface corrections on retrieval of bottom depth and reflectance using a semi-analytical model: A case study in Kaneohe Bay, Hawaii," *Appl. Opt.*, vol. 47, no. 28, pp. F1–F11, 2008.

[33] D. K. Clark, H. R. Gordon, K. J. Voss, Y. Ge, W. Wroenkow, and C. Trees, "Validation of atmospheric correction over the oceans," *J. Geophysical Res.*, vol. 102, no. D14, pp. 17209–17217, 1997.

[34] E. J. Botha, V. E. Brando, and A. G. Dekker, "Effects of per-pixel variability on uncertainties in bathymetric retrievals from high-resolution satellite images," *Remote Sens.*, vol. 8, no. 6, pp. 459–476, 2016.

[35] H. R. Gordon *et al.*, "Semianalytic radiance model of ocean color," *J. Geophysical Res. Atmos.*, vol. 93, no. D9, pp. 10909–10924, 1988.

[36] H. R. Gordon, "Dependence of the diffuse reflectance of natural waters on the sun angle," *Limnol. Oceanogr.*, vol. 34, no. 8, pp. 1484–1489, 1989.

[37] A. Morel and B. Gentili, "Diffuse reflectance of oceanic waters—II: Bidirectional aspects," *Appl. Opt.*, vol. 32, no. 33, pp. 6864–6879, 1993.

[38] Z. Lee, K. L. Carder, C. D. Mobley, R. G. Steward, and J. S. Patch, "Hyperspectral remote sensing for shallow waters—I: A semianalytical model," *Appl. Opt.*, vol. 37, no. 27, pp. 6329–6338, 1998.

[39] Y. Liu *et al.*, "Multispectral bathymetry via linear unmixing of the benthic reflectance," *IEEE J. Sel. Topics Appl. Earth Observ. Remote Sens.*, vol. 11, no. 11, pp. 4349–4363, Nov. 2018.

[40] DigitalGlobe, "Radiometric use of WorldView-2 imagery." Accessed: Sep. 20, 2019. [Online]. Available: https://dg-cms-uploads-production.s3.amazonaws.com/uploads/document/file/104/Radiometric_Use_of_WorldView-2_Imagery.pdf

[41] S. Jay and M. Guillaume, "Regularized estimation of bathymetry and water quality using hyperspectral remote sensing," *Int. J. Remote Sens.*, vol. 37, no. 2, pp. 263–289, 2016.

[42] R. A. Garcia, Z. Lee, and E. J. Hochberg, "Hyperspectral shallow-water remote sensing with an enhanced benthic classifier," *Remote Sens.*, vol. 10, no. 1, 2018, Art. no. 147.

[43] X. Huang, H. Chen, and J. Gong, "Angular difference feature extraction for urban scene classification using ZY-3 multi-angle high-resolution satellite imagery," *ISPRS J. Photogrammetry Remote Sens.*, vol. 135, pp. 127–141, 2018.

[44] H. Hirschmüller, "Stereo processing by semiglobal matching and mutual information," *IEEE Trans. Pattern Anal. Mach. Intell.*, vol. 30, no. 2, pp. 328–341, Feb. 2008.

[45] X. Huang, Y. Cao, and J. Li, "An automatic change detection method for monitoring newly constructed building areas using time-series multi-view high-resolution optical satellite images," *Remote Sens. Environ.*, vol. 244, 2020, Art. no. 111802.

[46] D. G. Lowe, "Distinctive image features from scale-invariant keypoints," *Int. J. Comput. Vision*, vol. 60, no. 2, pp. 91–110, 2004.

[47] B. Cao, Y. Fang, Z. Jiang, L. Gao, and H. Hu, "Shallow water bathymetry from WorldView-2 stereo imagery using two-media photogrammetry," *Eur. J. Remote Sens.*, vol. 52, no. 1, pp. 506–521, 2019.

[48] E. P. Green, P. J. Mumby, A. J. Edwards, and C.D. Clark, "Remote sensing handbook for tropical coastal management," in *Proc. UNESCO*, 2000, p. 34.

[49] CCRS Canadian Center for Remote Sensing, Accessed: Jun. 12, 2013. "Fundamentals of remote sensing." [Online]. Available: http://www.ccrs.nrcan.gc.ca

[50] D. Tanre, J. I. Deuze, M. Herman, R. Santer, and E. Vermote, "Second simulation of the satellite signal in the solar spectrum—6S code," in *Proc. 10th Annu. Int. Symp. Geosci. Remote Sens.*, 1990, p. 187.

[51] J. D. Hedley, A. R. Harborne, and P. J. Mumby, "Technical note: Simple and robust removal of sun glint for mapping shallow-water benthos," *Int. J. Remote Sens.*, vol. 26, no. 10, pp. 2107–2112, 2005.

[52] Y. Liu *et al.*, "Rapid estimation of bathymetry from multispectral images without in situ bathymetry data," *Appl. Opt.*, vol. 58, no. 27, pp. 7538–7551, 2019.

[53] J. Z. Ye, "Environmental hydrologic features of the Xisha arc-hipelago," in *Proc. Acta Scientiarum Naturalium Universitatis Sunyatseni*, vol. 35, pp. 15–21, 1996.

[54] The Free Dictionary, "Paracel islands." Accessed: Aug. 18, 2019. [Online]. Available: https://encyclopedia.thefreedictionary.com/Paracel+Islands

[55] South Surveying and Mapping Technology Company Limited, "Products solutions—SDE-28S+." Accessed: May 6, 2020. [Online]. Available: https://southinstrument.com/product/details/pro_tid/1/id/32.html

[56] P. T. Higgins, A. H. Choi, Y. Chen, J. C. Fondeur, P. Li, and J. Tian, "Bi-directional reflectance distribution function (BRDF)." Accessed: Jan. 6, 2020. [Online]. Available: http://www2.cs.arizona.edu/classes/cs433/fall08/lectures/BRDFandGlobalIllum.pdf

[57] A. G. Dekker *et al.*, "Imaging spectrometry of waters," in *Proc. Imag. Spectrometry, Basic Princ. Prospective Appl.*, 2002, pp. 307–359.

[58] U.S. Army Corps Eng., Eng. Des., Remote Sensing, Manual 1110-2-2907, Oct. 2003.

[59] B. Cao, R. Deng, and S. Zhu, Universal algorithm for water depth refraction correction in through-water stereo remote sensing, *Int. J. Appl. Earth Observ. Geoinf.*, vol. 91, 2020, Art. no. 102108.

Ruru Deng received the B.S. degree in geology from the Wuhan College of Geology, Wuhan, China, in 1984, the M.E. degree in remote sensing geology from the China University of Geosciences, Wuhan, China, in 1989, and the Ph.D. degree in microwave remote sensing from the Institute of Remote Sensing and Digital Earth, Chinese Academy of Sciences, Beijing, China, in 2002.

He is currently a Professor with Sun Yat-sen University, Guangzhou, China. His research interests include atmospheric correction of optical remote sensing data, quantitative remote sensing of inland waters and coral reefs, and cutting-edge development of microwave remote sensing.

Shulong Zhu received the B.E. degree in aerial photogrammetry, and the M.E. and Ph.D. degrees in photogrammetry and remote sensing from the Zhengzhou Institute of Surveying and Mapping, Zhengzhou, China, in 1988, 1993, and 1997, respectively.

He is currently a Professor in applied remote sensing with the College of Data Sciences, Information Engineering University, Zhengzhou, China. His current research interests include satellite photogrammetry, image understanding, pattern recognition, and RS-based bathymetry.
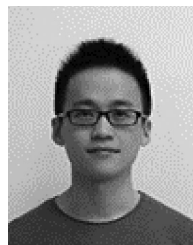
Yongming Liu received the B.S. degree from the China University of Geosciences, Wuhan, China, in 2014 and the Ph.D. degree in cartography and geographic information system from Sun Yat-sen University, Guangzhou, China, in 2019.

He is currently a Postdoctoral Researcher with the South China Sea Institute of Oceanology, Chinese Academy of Sciences, Guangzhou, China. His research interests include remote sensing of coral reefs and inland waters.

Yeheng Liang received the B.S., M.S., and Ph.D. degrees from Sun Yat-sen University, Guangzhou, China, in 2010, 2012, and 2016, respectively, all in geographic information systems.

He is currently an Associate Research Fellow with the School of Geography and Planning, Sun Yat-sen University. His research focuses on the inversion of heavy metals in water from satellite images.

Bin Cao received the B.E. degree in electronic and information engineering from Zhengzhou University, Zhengzhou, China, in 2015 and the M.E. degree in environmental science and engineering from Shanghai Ocean University, Shanghai, China, in 2018. He is currently working toward the Ph.D. degree with the School of Geography and Planning, Sun Yat-sen University, Guangzhou, China.

His research interests include applied optical remote sensing and satellite-derived bathymetry.

Longhai Xiong received the B.S. degree in geographic information systems from the North China University of Water Resources and Electric Power, Zhengzhou, China, in 2011, and the M.S. degree in marine geography and the Ph.D. degree in cartography and geographic information systems from Sun Yat-sen University, Guangzhou, China, in 2013 and 2018, respectively.

His research interests include surface water extraction, estimation of river runoff, soil moisture, and groundwater depth using remote sensing.